Published in final edited form as:
J Urol. 2010 October ; 184(4): 1514–1520. doi:10.1016/j.juro.2010.05.091.

Magnetic Resonance-Guided Focal Laser-Induced Interstitial Thermal Therapy in a Canine Prostate Model

R. Jason Stafford[*], **Anil Shetty**, **Andrew M. Elliott**, **Sherry A. Klumpp**, **Roger J. McNichols**, **Ashok Gowda**, **John D. Hazle**, and **John F. Ward**
Departments of Imaging Physics (RJS, AS, AME, JDH), Veterinary Medicine and Surgery (SK), and Urology (JFW), The University of Texas M. D. Anderson Cancer Center, Houston, Texas, and BioTex, Inc., Houston, Texas (RJM, AG)

Abstract

Purpose—To evaluate a newly FDA-cleared closed-loop, magnetic resonance (MR)-guided laser-induced interstitial thermal therapy (LITT) system for targeted ablation of prostate tissue in order to assess targeting ability, lesion generation and feasibility.

Materials and Methods—Mongrel dogs with (n = 2) and without (n = 5) canine transmissible venereal tumors in the prostate were imaged with a 1.5-T MR imaging scanner. Real-time 3D MR imaging was used to accurately position water-cooled 980-nm laser applicators to pre-determined targets within the canine prostates. Destruction of targeted tissue was guided with MR temperature imaging in real time for precise control of thermal ablation. MR predictions of thermal damage were correlated with findings from post-treatment images and compared to histopathology.

Results—Template-based targeting using MR guidance allowed the laser applicator to be placed within a mean of 1.1 mm (SD = 0.7 mm) of the target location. The mean width and length of the ablation zone by MR were 13.7 mm (SD = 1.3 mm) and 19.0 mm (SD = 4.2 mm) using single and compound exposures. The thermal damage predicted by MR correlated with the thermal damage determined by post-treatment imaging with a slope near unity and excellent correlation (R^2 = 0.94).

Conclusions—This LITT system provided rapid and localized heating of tissue with minimal collateral thermal spread or injury. Combined with real-time monitoring and template-based planning, MR-guided LITT is an attractive modality for prostate cancer focal therapy.

Keywords

Prostate Neoplasms; Laser Therapy; Image-guided surgery; Magnetic Resonance Imaging

INTRODUCTION

Radical prostatectomy and radiation therapy remain the gold standard therapeutic option for men with newly diagnosed prostate cancer [1, 2], but through increased awareness and screening with serum PSA, prostate cancers are being detected at an earlier stage. Radical whole gland therapy, whether by surgery or radiation, may not be necessary in all men with newly diagnosed prostate cancer to achieve equivalent cancer control. Data from NCI's SEER confirm the decline in stage diagnosis between 1974–1985 and 1995–2000[3, 4]. For this growing population of low- and intermediate-risk prostate cancer patients, active

[*]Correspondence: R. Jason Stafford, Ph.D., Department of Imaging Physics, Unit 56, The University of Texas M. D. Anderson Cancer Center, 1515 Holcombe Blvd., Houston, TX 77030-4009 (Telephone: 713.563.5082; FAX: 713.745.8547; jstafford@mdanderson.org).

surveillance may be undesirable, yet the short- and long-term complications and co-morbidities associated with radical whole-organ therapies still present unacceptable risks. Thus, there has been a growing interest in image-guided minimally invasive focal therapies, such as cryotherapy or high-intensity focused ultrasound (HIFU), for prostate carcinoma in select patients [5–9].

Laser-induced interstitial thermal therapy (LITT) is a minimally invasive modality for targeted tissue coagulation. Improvements in the design of high-power diode laser sources have made medical laser systems smaller, more portable, more powerful, and less expensive than previous generations. Water-cooled applicators now facilitate application of higher powers for rapid creation of larger ablation zones without tissue charring. Additionally, because LITT is magnetic resonance (MR) compatible, it may confer an imaging advantage over techniques utilizing transrectal ultrasound to target and monitor treatment [10] as MRI provides excellent soft-tissue anatomy and 3D acquisitions in any arbitrary orientation for treatment planning and targeting [11, 12] which has lead to the desire to incorporate prostate MRI into planning for external-beam radiotherapy and brachytherapy [13]. In addition to planning and verification, MR temperature imaging (MRTI) facilitates real-time temperature feedback during therapy [14, 15]. Emerging prostate MRI techniques, such as spectroscopic, diffusion, and perfusion imaging may potentially provide even better targeting of therapy, particularly at higher fields [11, 12]. MR-guided ablation technologies, such as LITT, have the potential to capitalize upon these advantages.

In this work, we evaluated an FDA-cleared, closed-loop, MR-guided LITT system for targeted ablation of prostate tissue using a canine prostate model. Specifically, we evaluated the performance of a transperineal grid for targeting locations in the prostate under MR guidance, measured the size of the ablation zones generated, and determined the correlation of tissue damage estimates based on MRTI with post-treatment imaging and histological verification.

MATERIALS AND METHODS

ANIMALS AND PROSTATE TUMOR MODEL

All procedures were performed at The University of Texas M. D. Anderson Cancer Center in accordance with the guidelines of the Institutional Animal Care and Use Committee. Seven adult male purpose-bred mongrel dogs (weighing ~20 kg) were used (source: The University of Texas Health Science Center, Houston, TX). Two dogs were immunosuppressed using cyclosporine and the left lobe of the prostate inoculated with 0.5 cm^3 of fresh canine transmissible venereal tumor (cTVT) fragments. After inoculation, tumors were monitored using MRI and allowed to grow for 6–8 weeks prior to treatment (~1 cm diameter).

For imaging and treatment, anesthesia was induced with intramuscular meditomidine (10 mg/kg) and maintained by inhalation of 2% isoflurane in O_2. In seven animals, a total of 11 ablations (9 in normal prostate and 2 in tumor), were performed under MR guidance.

MR-GUIDED LITT PROCEDURE

Briefly, anesthetized dogs were placed supine on a 4-channel, receive-only torso array coil in a 1.5 T clinical MR scanner (Excite HD, GE Healthcare, Waukesha, WI) and secured to minimize motion. Applicators were surgically inserted into the prostate of the 2 tumor-inoculated dogs via a laparotomy procedure. In the remaining 5 dogs, an MR-compatible perineal template grid with MR-visible markers was used to facilitate a targeted transperineal approach. Template software for the grid fused 3D MR anatomical images with a graphical representation of the grid openings to target locations in the prostate and

guide applicator placement, verified using T1-weighted images, and the error in placement measured (fig. 1). The plexiglass template was 7.6-cm × 7.6-cm × 1.3-cm thick to maintain accurate directional driving of the applicator through any of the 7×5 array of 1.6-mm diameter holes of the template face. Three water-filled fiducial markers, two on the face plate and a third on the plexiglass rod offset from the faceplate, were scanned prior to treatment and their 3D spatial locations recorded by the software. This positioning was then used to project the locations of the 7×5 array onto the treatment zone of the prostate as visualized by MRI.

The Visualase Thermal Therapy System (Visualase, Inc., Houston, TX) combines a therapeutic laser and cooled-catheter applicator with an image processing workstation for real-time MRTI-guided laser thermal therapy [15, 16]. A 15-W, 980-nm diode laser supplies energy to a 400-μm core diameter silica fiber-optic with a 1-cm long light-diffusing tip. The fiber is housed inside a 12-m long, 1.65-mm diameter coaxial cooling catheter connected to a peristaltic pump that circulates sterile saline to cool both applicator and the adjacent tissue.

The workstation read anatomical images from the scanner for placement of critical temperature control points for planning. High temperature control points (90ºC–95 ºC threshold) were placed on the image near the applicator-tissue interface to minimize deleterious high-temperature effects (charring, vaporization, and cavitation), which would limit the size of the ablation zone and possibly damage the applicator. When temperature exceeded this preset limit, treatment was terminated while tissue was allowed to cool, then treatment resumed until lesion was desired size (as observed on the workstation). Low temperature control points (45ºC–50ºC threshold) could be set near critical structures, such as the urethra, to minimize risk of damage. Exposure times in this study (<240-sec) and powers (4–14 W) were controlled using the workstation interface during treatment. Longer “compound” ablation zones were generated by pulling the fiber back within the applicator and re-exposing.

During treatment, real-time MRTI using the temperature-dependent proton resonance frequency shift technique [17] was used to monitor treatment progression via phase-sensitive gradient-echo images every 5-sec. The workstation calculated temperature from the gradient-echo images using a temperature sensitivity coefficient of −0.0097ppm/ºC, and displayed results on a 19” display. Damage was estimated from temperature using an integral Arrhenius method [16], which the workstation displayed as an orange region superimposed on the anatomical images.

PATHOLOGICAL ANALYSIS

After treatment, dogs were necropsied and prostates were extirpated and immediately fixed in 10% buffered formalin 5–7 days prior to sectioning. Based on the 3D T1-weighted MRI, fixed prostate specimens were sectioned along planes nearly congruent with the treatment plane and high-resolution digital photographs of sections obtained. Sections were stained with hematoxylin and eosin (H&E) and a polyclonal rabbit anti-human von Willebrand Factor (vWF) antibody (Dako, Carpinteria, CA) to evaluate vascular damage. Stained sections were scanned using a NanoZoomer Digital Pathology System (Olympus America, Center Valley, PA, a subsidiary of Hamamatsu Photonics, Japan) and a board-certified veterinary pathologist (SK) independently identified the borders of thermal necrosis for ablation zones.

RESULTS

MR-COMPATIBLE TEMPLATE AND TARGETING SOFTWARE

Ten locations where applicators were placed in the normal prostates of 5 dogs were targeted using the grid, and the error in placement measured from 3D anatomical MRI. The mean (± SD) radial placement error was 1.1 mm ± 0.7 mm (range 0.5 mm–2.9 mm) at a mean (± SD) depth of 50.7 mm ± 6.8 mm. Because the first applicator tended to stabilize the prostate, placement errors were statistically different for the second applicator (0.7 mm ± 0.2 mm, range 0.5 mm–1.1 mm) than for the first (1.5 mm ± 0.7, range 0.45 mm–2.9 mm) via a two-tailed Student's t-test assuming unequal variances ($p < 0.015$).

MR-GUIDED LITT

To test treatment delivery and guidance using the temperature monitoring, 11 ablation zones with a mean width of 13.7 mm ± 1.3 mm (range 11.4–15.5 mm) and mean length of 19.0 mm ± 4.2 mm (range 12.4–26.7 mm) were generated using single and compound exposures with power levels ranging from 4W to 14 W and maximum single exposures of up to 240 seconds (table 1). Average exposure time per site was 158 seconds, and average energy delivered was 995 J. For longer ablation zones, the fiber was moved back in the applicator 5–7 mm between exposures.

Using the workstation software for monitoring (fig. 2) with a 90ºC–95ºC threshold near the fiber, no charring or vaporization was observed on the applicator or at pathology. Temperatures at the margins of the ablated zone ranged between 54ºC–60ºC. Arrhenius-estimated tissue damage areas derived from MRTI were correlated with the outer rim of enhancement on 3D T1-weighted post-contrast images in the same plane to determine the degree of agreement with excellent correlation (Pearson's $R^2 = 0.94$, fig. 3). As desired, the slope of the regression line was close to unity ($m = 0.96$) and the intercept ($b = 8.44\ mm^2$) was small relative to the smallest ablation area measured ($115\ mm^2$). Mean discrepancy between Arrhenius versus T1-weighted measurement was −0.28% ± 7.6%, with an absolute error of 5.5% ± 4.9%.

PATHOLOGICAL ANALYSIS

Morphologic and histologic changes observed in the prostate were similar in all dogs and were consistent with previously reported descriptions of thermal damage in the prostate in that three distinct zones were observed (fig. 4) [14, 15]. On H&E-stained sections, each ablation zone appeared as a thermally fixed zone (TFZ) of unviable tissue surrounded by a pale coagulative zone of necrosis (CZN) and a marginal zone (MZ) transitioning into an untreated zone (UZ) of tissue.

Cellular changes varied between the TFZ, the CNZ and the outer MZ. Cellular and architecture features were retained in the TFZ adjacent to the site of the probe; the only morphological change was uniformly dark shrunken nuclei. Artifactual elongation and polarization of cells directly adjacent to the tract were induced by heat intensity from the probe (fig. 5). This phenomenon of "thermal fixation" has been documented in the prostate and various other tissues [14].

Parenchyma contained within the injured CNZ was characterized by loss of architectural detail. Cellular outlines were retained but cytoplasmic and nuclear details were obscured. Interstitial edema was also noted primarily adjacent to the MZ.

Morphological changes in the MZ were only discernable at high magnification. Cellular changes in the MZ consisted of multifocal sloughing of epithelial cells primarily adjacent to

the CNZ with retention of cellular architecture, uniformly small dark nuclei and edema of the interstitium. The width of the MZ varied with measurements between 0.5 and 2.5 mm.

Endothelial cells were immunostained for vWF (fig. 6). Acute thermal injury of blood vessels was observed especially within the MZ. The extent of vasculature injury determined whether plasma and/or plasma and blood cells leaked into the interstitium, which in turn resulted in edema and/or hemorrhage, respectively. Vascular injury was peracute and no disruption or necrosis of the endothelial cells was observed. vWF is also contained in plasma and within α-granules of platelets, resulting in immunopositive staining of the interstitium surrounding thermally injured vasculature.

DISCUSSION

Ideally, focal therapies for prostate cancer should have good visualization of the target and surrounding critical structures, an accurate method for delivering the applicator/energy, real-time monitoring of therapeutic effect, and reliable methods to protect surrounding critical structures. It has been well documented that the endorectal MRI provides better visualization of prostate anatomy and associated critical structures for treatment planning than either transrectal ultrasound or computed tomography,[10, 13] and while much work is still needed, MRI is the definitive imaging modality for early detection of initial or locally recurrent prostate cancer [18]. In this work, we demonstrated that by using a perineal grid template, one can use MRI to accurately (< 3mm) target locations within canine prostate and provide controlled LITT delivery.

The actively cooled applicator coupled with MRTI monitoring facilitated prostate ablation using a wide range of powers (4 W–14 W) for up to 240-sec without charring or vaporizing tissue; the control points helping to maintain a safe upper limit on the temperature near the applicator. Rapid tissue coagulation of regions up to 23 mm × 15 mm × 15 mm in size during a single exposure (14 W for 40 seconds) was feasible. Ablation zone length could be increased (up to 26 mm in this work) by simply moving the fiber within the applicator, a technique that might be useful for customizing treatments to the anterior part of the prostate while treating from the cranial to caudal aspect of the gland.

Additionally, Arrhenius-estimated tissue damage predictions from the MRTI allowed real-time visualization of the estimated ablation zone, allowing us to terminate the treatment when the ablation zone ceased to grow or when it grew too close to a critical structure as observed on anatomical MRI. While the size of the ablation zone could not be directly correlated with the exposure time and power level, the cumulative Arrhenius-estimated tissue damage prediction (fig. 3) provided excellent correlation with the outer edge of edema as observed on post-treatment contrast-enhanced 3D T1-weighted treatment verification imaging, indicating its potential use as a surrogate for this technique. This is important as several ablations can be performed and reliably predicted before administering contrast at the end of the study for verification.

However, there were some study limitations. We could not image temperature changes in adipose tissue [19] so in cases where the ablation zone was generated near the edge of the capsule adjacent to surrounding adipose tissue, temperature information was not available and tissue damage region was underestimated. For instance, in the left lobe of dog 4 in site A, extracapsular damage in adipose tissue could not be measured (table 1), so this data point was not included in the analysis (fig. 3).

Our pathological analysis strongly supported the detailed pathological analysis of ultrasound-induced thermal damage presented previously by Boyes et al.[17] H&E staining revealed the familiar region of thermal fixation, which leaves the treated tissue appearing

almost as if untreated, but with subtle changes [20, 21]. Outside the TFZ was a pale ring of necrosis transitioning quickly (less than 3 mm) to untreated tissue. The vWF immunostaining gave some insight into the impact of thermal therapy on the vasculature in the prostate. Acute LITT injury caused damage to some vessels, especially those within the pale band of necrosis and the less distinct MZ seen with H&E staining. Leakage from these injured interstitial vessels resulted in edema with immunopositive staining (brown) of both plasma and platelets containing von Willebrand Factor. Vascular disruption tended to extend slightly beyond the CNZ into the MZ in most cases, often following the vasculature. This effect could be useful if this thermal therapy is coupled with vascularly targeted therapies to treat microscopic disease in the periablational zone.

CONCLUSIONS

We demonstrated the transperineal MR-guided LITT system's ability to target and ablate regions in the prostate under real-time guidance in a canine prostate model. A transperineal template with MR-visible markers and registration software provided an excellent means for targeting the prostate tissue in the MR environment. MRTI feedback returned useful information that correlated well with post-treatment imaging and was predictive of the region of necrosis observed on pathology. Based on these results, advancement to investigation in humans is warranted.

Acknowledgments

This work was supported, in part, by NIH grant R44AG019276 (to BioTex, Inc.). The authors thank MR imaging technologists Krista Runge and Brandy Reed for their expertise in the execution of this research.

References

1. Menon M, Tewari A, Peabody JO, et al. Vattikuti Institute prostatectomy, a technique of robotic radical prostatectomy for management of localized carcinoma of the prostate: experience of over 1100 cases. Urol Clin North Am. 2004; 31:701. [PubMed: 15474597]
2. Hakimi AA, Feder M, Ghavamian R. Minimally invasive approaches to prostate cancer: a review of the current literature. Urol J. 2007; 4:130. [PubMed: 17987573]
3. Jemal A, Siegel R, Ward E, et al. Cancer statistics, 2007. CA Cancer J Clin. 2007; 57:43. [PubMed: 17237035]
4. Silverberg E, Boring CC, Squires TS. Cancer statistics, 1990. CA Cancer J Clin. 1990; 40:9. [PubMed: 2104569]
5. Ward JF, Nakanishi H, Pisters L, et al. Cancer ablation with regional templates applied to prostatectomy specimens from men who were eligible for focal therapy. BJU Int. 2009
6. Gonzalgo ML, Patil N, Su LM, et al. Minimally invasive surgical approaches and management of prostate cancer. Urol Clin North Am. 2008; 35:489. [PubMed: 18761202]
7. Zerbib M, Zelefsky MJ, Higano CS, et al. Conventional treatments of localized prostate cancer. Urology. 2008; 72:S25. [PubMed: 19095125]
8. Moul JW, Mouraviev V, Sun L, et al. Prostate cancer: the new landscape. Curr Opin Urol. 2009; 19:154. [PubMed: 19195129]
9. Marberger M, Carroll PR, Zelefsky MJ, et al. New treatments for localized prostate cancer. Urology. 2008; 72:S36. [PubMed: 19095127]
10. Jolesz FA, Hynynen K, McDannold N, et al. MR imaging-controlled focused ultrasound ablation: a noninvasive image-guided surgery. Magn Reson Imaging Clin N Am. 2005; 13:545. [PubMed: 16084419]
11. Puech P, Huglo D, Petyt G, et al. Imaging of organ-confined prostate cancer: functional ultrasound, MRI and PET/computed tomography. Curr Opin Urol. 2009; 19:168. [PubMed: 19188771]
12. Kurhanewicz J, Vigneron D, Carroll P, et al. Multiparametric magnetic resonance imaging in prostate cancer: present and future. Curr Opin Urol. 2008; 18:71. [PubMed: 18090494]

13. McLaughlin PW, Troyer S, Berri S, et al. Functional anatomy of the prostate: implications for treatment planning. Int J Radiat Oncol Biol Phys. 2005; 63:479. [PubMed: 16168840]

14. Boyes A, Tang K, Yaffe M, et al. Prostate tissue analysis immediately following magnetic resonance imaging guided transurethral ultrasound thermal therapy. J Urol. 2007; 178:1080. [PubMed: 17644137]

15. Hazle JD, Diederich CJ, Kangasniemi M, et al. MRI-guided thermal therapy of transplanted tumors in the canine prostate using a directional transurethral ultrasound applicator. Journal of Magnetic Resonance Imaging. 2002; 15

16. McNichols RJ, Gowda A, Kangasniemi M, et al. MR thermometry-based feedback control of laser interstitial thermal therapy at 980 nm. Lasers Surg Med. 2004; 34:48. [PubMed: 14755424]

17. Rieke V, Butts Pauly K. MR thermometry. J Magn Reson Imaging. 2008; 27:376. [PubMed: 18219673]

18. Sartor AO, Hricak H, Wheeler TM, et al. Evaluating localized prostate cancer and identifying candidates for focal therapy. Urology. 2008; 72:S12. [PubMed: 19095124]

19. de Zwart JA, Vimeux FC, Delalande C, et al. Fast lipid-suppressed MR temperature mapping with echo-shifted gradient-echo imaging and spectral-spatial excitation. Magn Reson Med. 1999; 42:53. [PubMed: 10398950]

20. Wu F, Wang ZB, Cao YD, et al. Heat fixation of cancer cells ablated with high-intensity-focused ultrasound in patients with breast cancer. Am J Surg. 2006; 192:179. [PubMed: 16860626]

21. Coad JE, Kosari K, Humar A, et al. Radiofrequency ablation causes ‘thermal fixation’ of hepatocellular carcinoma: a post-liver transplant histopathologic study. Clin Transplant. 2003; 17:377. [PubMed: 12868996]

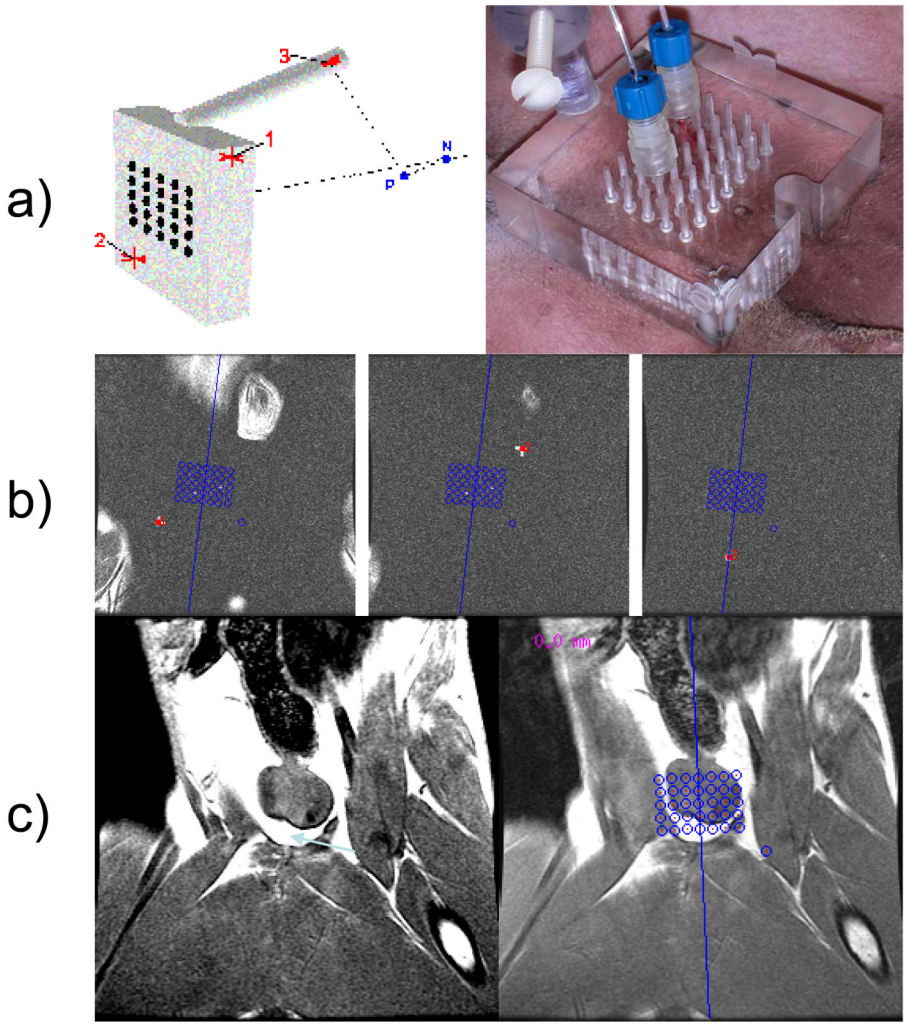

Figure 1.

Planning of applicator placement with template guidance. *A*, Diagram of the perineal template demonstrating the location of the 3 MR-visible markers for registration (left) and the actual template on the perineum with 2 laser applicators placed in the prostate (right). *B*, Appearance of the 3 MR-visible markers on 3D T1-weighted images. *C*, An image of the prostate with (right) and without (left) the template grid overlay.

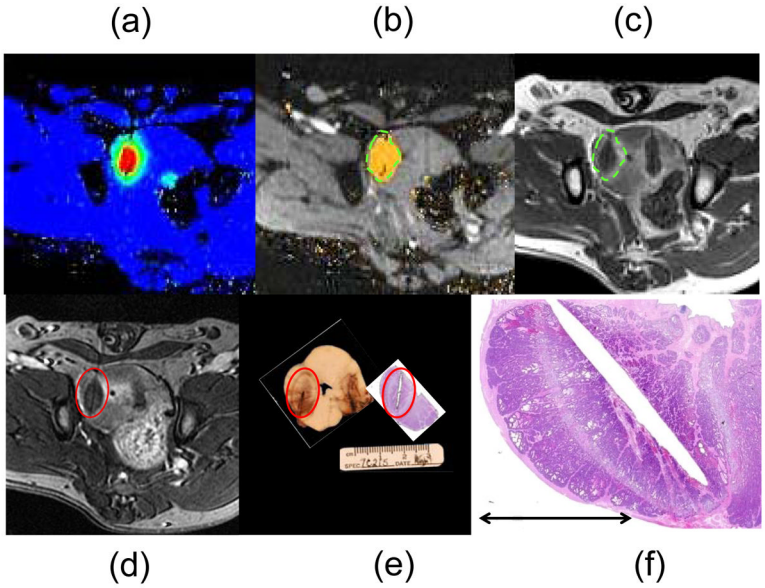

Figure 2.

MR-guided LITT in a canine prostate model. MR temperature imaging from the LITT workstation displays the temperature changes in the prostate in real time (*A*), is used to estimate and display the TNZ (*B*), which correlates well with the outer edge of the ring of edema seen surrounding a non-perfused region of tissue on post-treatment (less than 20 minutes) 3D T1-weighted contrast-enhanced images (*C*). Dotted green lines show the edges of estimated tissue damage projected onto both images (*B* and *C*) for visual correlation. The images from (*C*) were reformatted (*D*) to better match the actual slices taken from photographic pathology and H&E histology, where the ablation zone is contained inside the red reference line (*E*). The histological damage demonstrated the classic presentation of thermal necrosis as described in the text, with a very narrow region of transition between normal and necrotic cells (*F*). Despite slight through-plane refraction and approximated slice orientations, excellent agreement was observed.

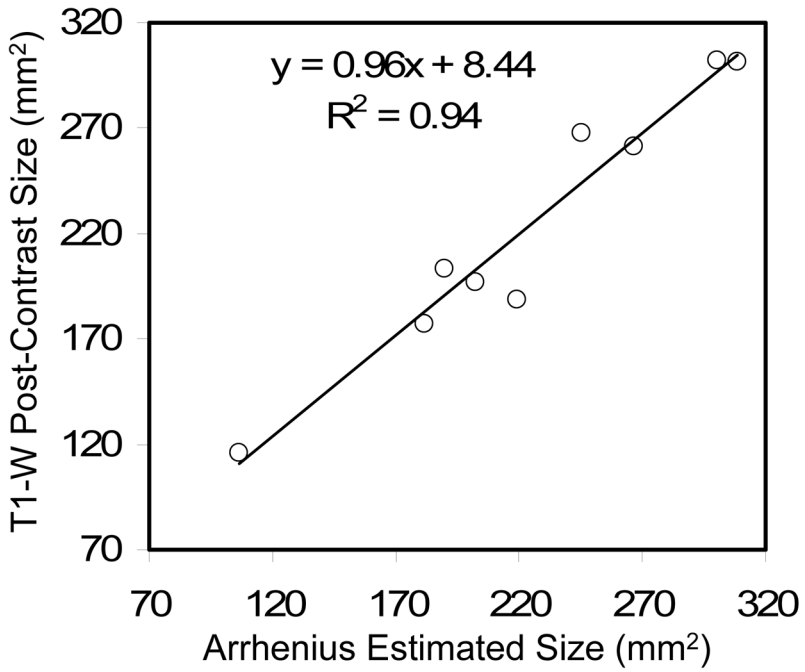

Figure 3.

Three-dimensional T1-weighted post-contrast measurements of LITT-induced ablation size (measured from the outer edge of edema) versus the Arrhenius-estimated tissue damage based on MR demonstrated excellent correlation. Linear least-squares regression indicates a slope near unity and a bias much smaller than the area of the smallest ablation zone measured.

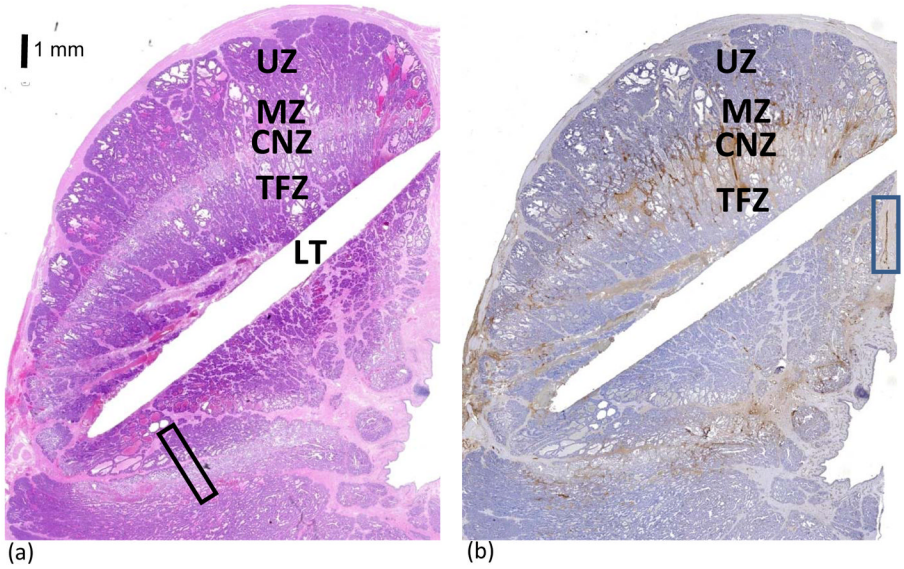

Figure 4.

Histological depiction of cellular changes in the ablation zone on H&E-stained sections (A) showed 3 distinct areas of unviable tissue: 1) the TFZ immediately surrounding the fiber, which was heat fixed and structurally intact; 2) the CNZ, which was a pale rim of coagulation necrosis surrounding the TNZ; and 3) the MZ, which was a less distinct thin band with edema in the interstitial tissue. See Figure 5 for higher magnification of the area within the rectangle (A). The chromogen diaminobenzidine tetrahydrochloride (DAB) is brown and allowed visualization of vWF immunolabeling (B). vWF immunostained endothelial cells. Immunopositive staining in the blue rectangle was endothelial cells lining an intact blood vessel. Abnormally excessive vWF immunostaining was seen adjacent to the laser tract as a result of traumatic injury, and in the CNZ and MZ due to thermally injured blood vessels resulting in edema derived from leakage of plasma and plalelets into the interstitial areas. LT= laser tract; TFZ= thermally fixed zone; CZN= coagulative necrosis zone; MZ= margin zone; and UZ= untreated zone. Bar = 1 mm.

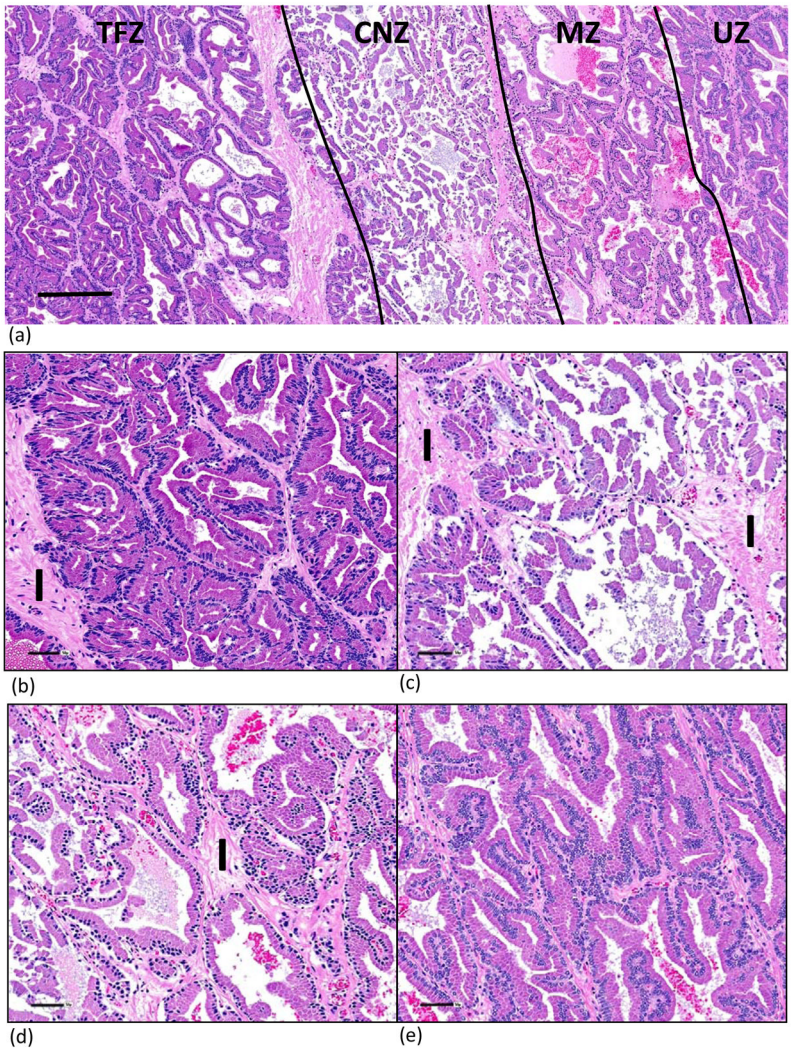

Figure 5.

H&E-stained section showing laser induced tissue damage. Higher magnification of rectangular area showing four zones identified in Figure 4A (A). Bar =250μ. TFZ showed intact architectural and cellular structures; the only morphologic abnormality was dark, shrunken, spindyloid to oval nuclei. Interstitium was normal and composed of compact collagen (B) The CNZ showed coagulation necrosis with retention of cellular outlines but loss of cytoplasmic and nuclear detail. Epithelial sloughing was evident. The interstitium on the left is normal; the interstitium on the right contains a dilated vein and loosely woven collagen due to plasma leakage from thermally damaged vessels (C). The primary changes in the MZ were edema (plasma leakage) of the interstitium, and uniformly dark shrunken nuclei. The MZ adjacent to the CNZ had sloughed epithelial cells and red blood cells in the lumens of glands. (D) The UZ is characterized by normal glandular and cellular architecture with open-faced nuclei (E). I = interstitium. Bar = 50μ (B–E).

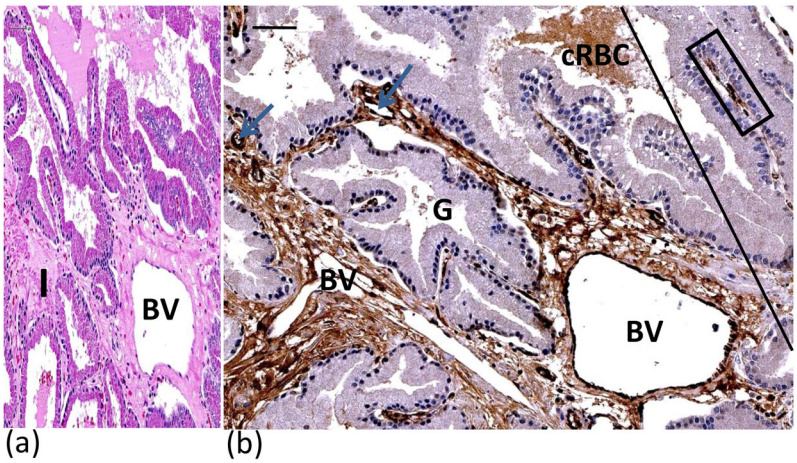

Figure 6.

H&E (A) and vWF immunostained (B) sections illustrated effects of vascular damage in MZ. H&E staining showed loosely woven collagen and expansion of interstitial tissue due to leakage of plasma from damaged blood vessels resulting in edema(A). MZ is to the left and UZ to the right of tangential line (B). Blue arrows point to blood vessels in the interstitium. Note dark brown staining of endothelial cells lining dilated blood vessel (BV). Interstitium immunopositive for vWF due to leakage of plasma into interstitium from thermally injured blood vessels. Crenated red blood cells and plasma within lumen of prostatic gland were immunopositive for vWF. Immunopositive endothelial cells lining an intact vein (within blue rectangle) in UZ with no edema in interstitium. BV = blood vessel; cRBC = crenated red blood cells; G= prostatic gland. Bars (upper left) = 50μ.

Table 1

Summary of MR-guided LITT exposure times and size of ablation zones generated in a cTVT canine prostate model

Subject	Lobe	Site†	Length (mm)	Width (mm)	Power (W)	Time (sec)	Tot. time (sec)	Energy (J)
1	R	A	12.4	13.8	(4, 4)‡	(114, 121)	235	940
1	L*	A B	21.2	13.4	(4, 4) 6	(182, 121) 59	362	1562
2	R*	A B C	26.7	12.9	(4, 6) (6, 6) (4, 4)	(121, 72) (39, 66) (106, 120)	524	2450
3	R	A	23.2	14.6	14.3	40	40	572
4	R	A	17.7	12.5	12	63	63	756
4	L	A	17.5	11.4	(12, 11.3, 6, 6)	(37, 37, 243, 190)	507	3460
5	R	A B	22.8	15.4	12.8 6.4	29 202	231	1664
5	L	A	19.1	14.9	6.4	71	71	462
6	R	A	16.5	15.5	(6, 12)	(32, 104)	136	1440
6	L	A	13.2	12.2	(6, 12)	(33, 74)	107	1086
7	R	A	19.2	14.0	6	90	90	540

*Exposures made in cTVT tissue.

†Different sites treated by pulling fiber back in applicator.

‡In cases where multiple exposures were performed to generate a larger/longer ablation zone, the power and exposure time are expressed as (Exposure 1, Exposure 2, …).